UNIVERSITY OF BIRMINGHAM

University of Birmingham
Research at Birmingham

Identifying heating rate dependent oxidation reactions on a nickel-based superalloy using synchrotron diffraction

Reynolds, Tom; Collins, David; Soor, Nicole; Street, Steven; Warnken, Nils; Mignanelli, Paul; Hardy, Mark; Evans, Hugh; Taylor, Mary

Link to publication on Research at Birmingham portal

Full length article

Identifying heating rate dependent oxidation reactions on a nickel-based superalloy using synchrotron diffraction

T.D. Reynolds[a]

D.M. Collins[a]

N.K. Soor[a]

S.R. Street[b, c]

N. Warnken[a]

P.M. Mignanelli[d]

M.C. Hardy[d]

H.E. Evans[a]

M.P. Taylor[a, *]

m.p.taylor@bham.ac.uk

[a]School of Metallurgy and Materials, University of Birmingham, Birmingham, B15 2TT, UK

[b]Overall Forge Pty Ltd, 70 R.W. Henry Drive, Ettamogah, NSW, 2640, Australia.

[c]School of Materials Science and Engineering, University of New South Wales, Sydney, New South Wales 2052, Australia

[d]Rolls-Royce, PO Box 31, Derby, DE24 8BJ, UK.

*Corresponding author.

Abstract

Synchrotron grazing incidence X-ray diffraction has been used to newly reveal the heating rate dependent oxidation reactions that develop on a polycrystalline nickel-based superalloy. A continuous layer of precursor oxide was shown to form during the heating stage. Their approximate growth rates, their effect on local surface compositions of the alloy substrate, and their degree of interface planarity are considered critical in determining subsequent oxidation reactions when held for extended thermal exposures. The precursor oxides were predominantly nickel or cobalt based (NiO/CoO and $Co_3O_4/NiCo_2O_4$). Following the fastest heating rates (40 $°C\,min^{-1}$ and above), the stable Cr_2O_3 phase formed, inhibiting Ni or Co diffusion to the surface. At slower heating rates (10–20 $°C\,min^{-1}$), no evidence of the stable Cr_2O_3 was found, even after 200 h at elevated thermal exposure, instead continued growth of the precursor oxides was observed. Heating at 5 $°C\,min^{-1}$ gave rise to an intriguing zone where sufficient precursor and favourable kinetics enabled the formation of a spinel, $NiCr_2O_4$, surface layer. Cross sections observed with electron microscopy confirmed this to be planar and continuous. Heating at the slowest tested 2 $°C\,min^{-1}$ contrarily gives a non-protective surface layer comprising an outwardly growing NiO/CoO precursor oxide on top of an inwardly growing mixed oxide. The quantities, interfacial morphologies of oxides of the precursor oxide grown and the possible thermodynamic reactions that lead to their formation are discussed.

Keywords: Synchrotron XRD; Oxidation; Ni-based superalloy

1 Introduction

The high temperature capability of nickel-based superalloys used in gas turbines is heavily determined by their resistance to oxidation. For a given alloy, the specific oxidation compounds that form are dependent on both the thermal environment and atmosphere subjected to the component in conjunction with its thermodynamic/kinetic properties that are intrinsic to the alloy itself. As both the compositions and thermal cycles observed by components in service are complex, ascertaining and understanding oxidation reactions is a key aspect of alloy development, as well as judicious selection of in-service conditions.

The oxidation process can be divided into the initial stages, a transitional stage, and finally, longer term steady state oxidation, where one or two oxides dominate. The resultant steady state oxidation is highly dependent on the prior stages; however, identifying behaviour changes is exceptionally challenging when oxidation layers are thin. Therefore, initiation stages or precursor oxides that form prior to steady state oxidation are not well characterised and the mechanisms are not unambiguously understood. This is especially true for nickel-base superalloys where alloy compositions are complex and components are subjected to transient high temperature thermal cycles.

The initial stages involve the adsorption of oxygen onto surfaces followed by a reaction between the cations and anions. These processes have been studied for some pure metals and simple alloy systems using exacting experimentation techniques; e.g. [1–9]. These studies involved monitoring the changes occurring to clean metallic surfaces when exposed to oxidising environments, using a number of high spatial resolution techniques. Such investigations have shown the initial adsorption step of the oxidising species to the surface of the metal followed by the nucleation of islands of oxide. Investigations of relevance to nickel-base superalloys, e.g. Ni-Cr binary alloys [5–7], demonstrated the formation of NiO islands interspersed with a Cr complex; when at very early stages of Cr_2O_3 formation. The studies all show that the nucleation and growth rates depend on a number of factors including crystal orientation at the exposed surface of the metal [2,3,4,5,8] and alloying additions [5–9]. These processes may occur rapidly in time periods of a few minutes or may extend to 90 min. Such carefully controlled experiments have yet to be performed on complex alloys but it would be expected that oxide islands would also form, with each island potentially composed of either a discrete oxide, a mixture of individual oxides, ternary or higher component stable or metastable oxide phases.

The steady state oxidation regime occupies much of the lifetime of metal and alloy components, making it of utmost interest to oxidation vulnerable engineering applications. At this stage in the oxidation process, the ease that oxidising elements diffuse through a growing surface oxide layer becomes a significant factor [10]. Investigations into the steady state oxidation of the nickel-based disc alloy of interest in this paper have been conducted [11–17] providing data for lifing models to predict, for instance, the onset of breakaway oxidation [18], or the loss of cross-section and mechanical integrity.

The transition from the initial processes of adsorption and nucleation to the steady state oxidation is difficult to define and can vary between metals and alloy systems [19]. A useful definition is; a region in the oxidation process where complete coverage of a surface oxide exists but that this layer comprises a mixture of oxides including stable and metastable phases. This oxide layer continues to have phase transformations and compositional changes but no single oxide dominates. In addition, this region can include thermal transients which introduce further factors for consideration.

The free energies of formation of the potential oxides are important, however, the kinetics of oxide growth play an increasing role in the establishment of the steady state reactions [19,20]. Often a number of oxides will be thermodynamically stable in alloy systems but each may possess very different kinetics, thus taking time before a slower growing protective oxide establishes, if this occurs at all. The stability of an oxide under these conditions will depend on the activity of the element within the alloy and also the partial pressure of the oxidant at the reaction sites. Similarly, the growth rate will be dependent on the supply of the oxidising element from the alloy and/or the oxidant to the reaction site, i.e. diffusion becomes an important factor [10,18].

An oxide type of relevance to the intermediate or transient stage in the oxidation process of nickel-based alloys are the spinels; with the formula MN_2O_4 where M, for most nickel-base superalloys, is nickel or cobalt and N is cobalt, chromium or aluminium. In alloys with sufficient aluminium $NiAl_2O_4$ spinels have been shown to form [21–26]. At lower temperatures, and on alloys with low concentrations of aluminium, $NiCr_2O_4$ would be the preferred composition [27–33]. Spinels can form by a solid state reaction between adjacent oxides or oxide and alloy [27–31]. An alternative mechanism may be via solute capture of alien ions within an oxide where concentrations substantially greater than the solubility levels in the oxide were achieved [32]. Capture of Ni ions within Cr_2O_3 and Cr ions within NiO have been demonstrated; this could be a precursor to a spinel reaction. With increased exposure at elevated temperature, a transient phase could transform to a spinel.

Models have been proposed to describe the oxide formation sequence involving spinels [19,20,21–24,29–31]. In these, the spinel phase is shown as a discontinuous layer hindering rather than controlling the oxidation process. A few studies have shown that the presence of a protective spinel layer impacts the oxidation kinetics, forming a more continuous layer for at least part of the thermal history of the specimen [25–27,30]. It is noted that in studies where a range of temperatures were investigated, a more continuous layer of spinel formed at the lower temperatures investigated, [25,26,29,31]. The concentration of chromium in the alloys was also shown to have an effect [7,19,25,29] as did low concentration elements such as molybdenum [9].

In a recent experiment [33] intended to examine the effect of elevated air pressure on the oxidation properties of a nickel-based superalloy, high-pressure tests resulted in the formation of a continuous external oxide layer of nickel chromite spinel ($NiCr_2O_4$) rather than the more usual titanium doped chromia, $(Ti, Cr)_2O_3$, observed at atmospheric-pressure [11–17]. This result was unexpected and was unlikely to be a result of the difference in test pressure. It was subsequently realised that an additional variable introduced into the experiment was the heating rate to the test temperatures of 650 °C. The purpose of this paper is to explore the effect of heating rate on the oxidation

formation and behaviour of a polycrystalline nickel-base superalloy. This was explored using a combination of microscopy and high angular resolution synchrotron X-ray diffraction in a grazing incidence configuration (SGIXD). This technique uniquely enabled the examination of very thin oxide layers formed during the transient oxidation stage.

2 Experimental methods

2.1 Material and sample preparation

The composition of the coarse-grained (30–50 μm) polycrystalline nickel-based superalloy used in this study, RR1000, is given in Table 1.

Table 1 Nominal composition of RR1000 [34].

alt-text: Table 1

	Ni	Co	Cr	Al	Ti	Ta	Hf	Zr	Mo	B	C
wt.%	bal.	18.5	15.0	3.0	3.6	2.0	0.5	0.06	5.0	0.015	0.027
at.%	bal.	16.5	18.0	6.4	4.3	0.63	0.16	0.04	3.0	0.08	0.13

Coupon specimens measuring 10 × 10 × 3 mm^3 were supplied in a proprietary heat-treated condition. The surfaces of the specimens were ground using successive SiC paper down to 1200 grit and polished using diamond suspension down to a 1 μm finish, as used in a previous study [33]. The edges of specimens were chamfered to reduce stress accumulation associated with oxide growth at corners. The specimens were ultrasonically cleaned in ethanol.

2.2 Oxidation tests

A tube furnace equipped with a programmable controller was used for all thermal exposures examined in this study. The temperature within the hot section was monitored independently using a calibrated N-type thermocouple. The heating rates chosen were 2, 5, 10, 20, 40 °C min^{-1} and nominally 'fast' (~100 °C min^{-1}), reaching the target temperature of 650 °C in <10 min. The heating rates were deliberately selected to both overlap and extend beyond the processing heat treatment and operating conditions typically to which this alloy is subjected.

Specimens were placed into alumina boats and inserted into the test furnace at room temperature, before heating at the desired rate to the target temperature of 650 °C. The specimens were removed from the furnace after the heating stage and stored. For the fastest heating rate used, the boat containing the specimens was inserted into the furnace at temperature and removed when the independent thermocouple indicated that the specimens and boat had reached 650 °C. For subsequent thermal exposures, the specimens were placed in alumina boats and inserted into furnaces set to 650 °C, i.e. the specimens experienced rapid heating to the test temperature and also rapid cooling to room temperature when removed. The conditions studied were; (1) a controlled heating rate to 650 °C followed by immediate air cooling when this temperature was reached, (2) fast heating to 650 °C, of specimens that had previously followed condition (1) then held for 100 h followed by air cooling, and (3) comprising an additional repeat of condition (2) i.e. 2 × 100 h exposures. Despite the thermal cycling, no spallation of oxide from the surface of the specimens was observed. An additional exposure was performed for 1000 h on specimens which had undergone the slowest heating rate of 2 °C min^{-1}. For completeness, a specimen of the alloy which had undergone the same surface preparation but had not been exposed to temperature was included for examination.

2.3 Synchrotron GIXD

When studying multiple low volume fraction phases with laboratory-based X-ray diffractometers, the intrinsic line broadening associated with this technique leads to significant reflection overlap. This, in addition to its low flux, prohibits the observation of weak reflections, making unambiguous phase identification impossible. These disadvantages are overcome by using synchrotron-based X-ray diffraction techniques. Here, ex-situ synchrotron grazing incidence X-ray diffraction (SGIXD) was employed to examine specimens using the high angular resolution powder diffraction beamline, I11 at the Diamond Light Source [35]. The SGIXD technique enabled the identification of the phases present in thin oxide layers formed during the early stages of oxidation.

An X-ray energy of 15 keV was selected with a wavelength of 0.824812 Å; calibrated against a NIST 640c Si standard. Specimens were positioned using adhesive carbon pads onto aluminium stubs and placed on the diffractometer stage in the grazing incidence geometry, shown schematically in Fig. 1. By visual inspection along the beam direction (x), the specimens were manually aligned via a ψ rotation about the x-axis, to correct sample orientation in the y-z plane. More precise positioning of the specimen in the z and θ directions was performed by a series of iterative alignment scans, using the X-ray beam.
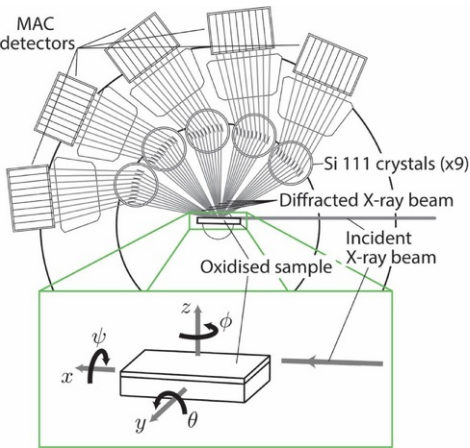
Figure Fig. 1 Schematic diagram of the SGIXD configuration on the I11 beamline showing the directions and axes of rotation used to align the specimen relative to the incident beam.

alt-text: Fig. 1

Diffraction patterns were obtained via a 2θ scan over the range 3°–150° using the high-resolution multi-analysing crystals (MAC), comprising 45 individual Si detectors grouped into 5 banks of 9 detectors. This enabled the full 2θ range to be scanned by 40° of motion, with overlap between detectors. Data from the 45 individual crystals were integrated to produce a final spectrum. In the initial set up various incident angles (obtained by the adjustment of θ about the y direction) and scan times were investigated. It was found that an incidence angle of 1° with a 30-minute scan time provided spectra of sufficient signal-to-noise ratio for interpretation. By default, spectra were binned into 2θ intervals of 0.001°. To improve the signal-to-noise ratio the data was re-binned into 0.01° intervals.

For phase identification, reference patterns were obtained from the Inorganic Crystal Structure Database (ICSD) [36]. This included patterns from expected oxides as well as a number of spinel phases selected by using a combination of the major elements present within the alloy. Details of the candidate phases and their structures are given in Table 2. Also included is the information on the γ (matrix) and γ′ (precipitate) major phases of the substrate. Examination of the data in Table 2 shows that some phases have similar crystal structures and lattice parameters that makes unambiguous identification, using this technique, impossible. Examples are Co_3O_4 and $NiCo_2O_4$ and also NiO and CoO. Due to this ambiguity the nomenclature Co_3O_4/$NiCo_2O_4$ and NiO/CoO will be used to indicate the peaks associated with these compounds. It is noted that $NiCr_2O_4$ undergoes a phase transformation at 46 °C from the higher temperature cubic structure to the lower temperature tetragonal structure [44]. The calculated 2θ positions and intensities for the major reflections for these oxides, using synchrotron radiation, are presented in Table 3.

Table 2 Room temperature crystallographic information for phases of interest in this study, obtained from the ICSD database [37–46].

alt-text: Table 2

Structure	Crystal system	Space group	a/b (Å)	c (Å)	α/β (°)	γ (°)	ICSD code
γ gamma	Cubic	$Fm\bar{3}m$	3.583	3.583	90	90	–
γ′ gamma prime	Cubic	$Pm\bar{3}m$	3.598	3.598	90	90	–
Cr_2O_3	Trigonal	$R\bar{3}c$	4.957	13.5923	90	120	75-577
$(Cr_{0.88}Ti_{0.12})_2O_3$	Trigonal	$R\bar{3}c$	4.97217	13.6343	90	120	74-195
TiO_2 (rutile)	Tetragonal	$P4_2/mnm$	4.6012	2.9637	90	90	257-864
NiO	Cubic	$Fm\bar{3}m$	4.178	4.178	90	90	9866
CoO	Cubic	$Fm\bar{3}m$	4.263	4.263	90	90	9865

Al_2O_3	Trigonal	$R\bar{3}c$	4.7617	12.999	90	120	160,604
Co_3O_4	Cubic	$Fd\bar{3}m$	8.072	8.072	90	90	36,256
$NiCr_2O_4$*	Tetragonal*	$I4_1/amd$	5.8102	8.4806	90	90	280,062
$NiCo_2O_4$	Cubic	$Fd\bar{3}m$	7.983	7.983	90	90	181,262
$CoCr_2O_4$	Cubic	$Fd\bar{3}m$	8.333	8.333	90	90	69,503

* $NiCr_2O_4$ undergoes a phase transformation at 46 °C from a high temperature cubic $Fd\bar{3}m$ to a room temperature tetragonal structure. [44].

Table 3 Peak location and intensities for relevant oxides.

alt-text: Table 3

NiO/CoO			Cr_2O_3			$Co_3O_4/NiCo_2O_4$			$NiCr_2O_4$		
(hkl)	2θ (°)	I/I_{max} (%)	(hkl)	2θ (°)	I/I_{max} (%)	(hkl)	2θ (°)	I/I_{max} (%)	(hkl)	2θ (°)	I/I_{max} (%)
{111}	19.7	73.5	(012)	13.1	66.7	{022}	16.5	26.9	(112)	16.1	35.8
{002}	22.8	100	(01$\bar{4}$)	17.8	100	{113}	19.4	100	(013)	18.7	47.0
{022}	32.4	62.0	(110)	19.2	93.5	{004}	23.5	20.0	(121)	19.1	100
{113}	38.2	30.7	(113)	21.9	29.0	{115}	30.6	26.0	(231)	30.2	30.2
			(024)	26.3	38.5	{044}	33.4	39.4	(224)	32.5	45.6
			(116)	28.6	97.4				(040)	33.0	22.1

The technique is used here to collect spectra from a number of specimens exposed to different heating rates and exposure times at 650 °C. As such, each spectrum contains information obtained from a different interaction volume. Due to this limitation, qualitative comparisons can be made between specimens but not quantitative.

2.4 Additional examination of specimens

Surfaces of selected specimens were examined using Scanning Electron Microscopy (SEM) in secondary electron mode. Compositional analysis was obtained using Energy Dispersive X-ray Spectroscopy (EDS). To investigate the surface oxide in cross-section, a Ga source Focused Ion Beam (FIB) milling was used. This was appropriate for the examination of the very thin, friable surface oxides formed which may be damaged using conventional cross-sectioning techniques. The technique also has the advantage of precise site selection.

3 Results

3.1 Evaluation of the heating rate on oxide formation

The spectra over the 2θ range of 10°–70°, plotted as the square root of the intensities, obtained from specimens following the heating stage only, are presented in Fig. 2 along with the spectrum obtained from the un-oxidised specimen included here for reference. For direct comparison of spectra over shorter 2θ ranges no modification was made. In all cases the baselines are off-set to distinguish between different diffraction patterns.
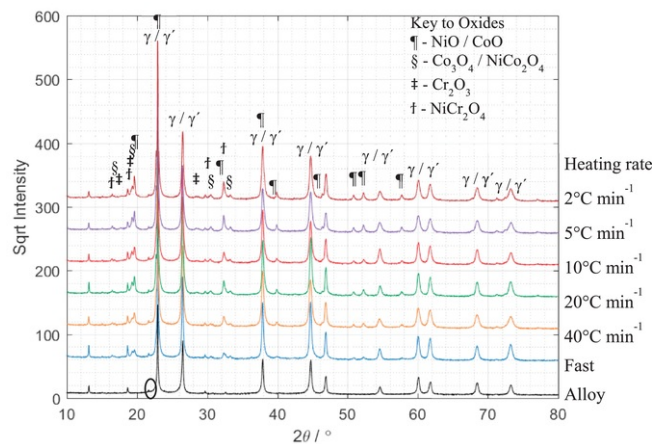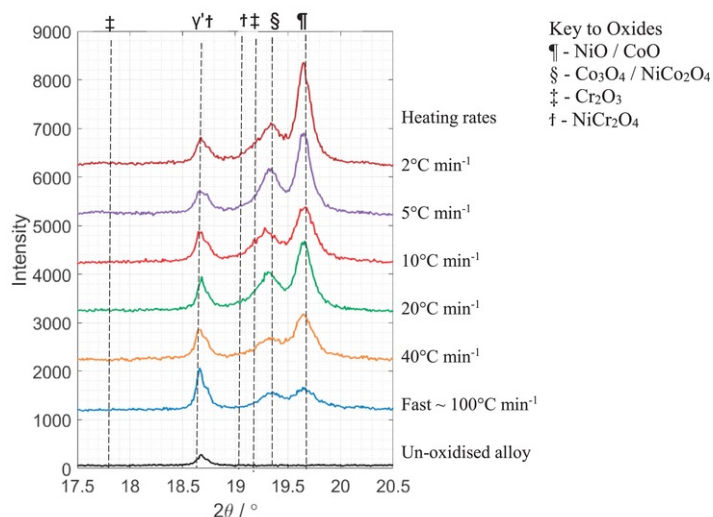
Figure Fig. 2 SGIXD spectra of alloy following exposure over the heating rates shown in the legend, labelled, and cooled to room temperature, including the spectrum from the un-oxidised specimen, revealing the additional peaks formed during the heating stage, identified as NiO/CoO and the Co_3O_4/$NiCo_2O_4$ spinel. Also, circled on the alloy spectrum, is an unidentified peak associated with the alloy and present in all traces.

alt-text: Fig. 2

It can be seen, by comparison to the un-oxidised specimen, labelled Alloy alloy in Fig. 2, that the highest intensity peaks were from the γ/γ' phases in the alloy substrate. Also, indicated at a 2θ of 21.8° was a peak that could not be indexed from any expected phase. The unidentified peak was observed in all the SGIXD spectra obtained in this study and was speculated to originate from a minor phase or oxide present in the alloy. It was not investigated further in this study. This peak and its location, as will be shown later, was sufficiently remote from the locations of the oxide peaks so as not to impact on the identification process.

Clashes in peak positions are inevitable when dealing with this type of data, as can be seen in Table 3. Thus, a comprehensive examination of the whole spectra was necessary. It was found that the ideal 2θ range for the major peaks of interest was between 17° to and 21°, Fig. 3, and includes the {011} γ' peak at 18.7°. As can be seen in Fig. 3, the resolution of the SGIXD data was sufficient to distinguish between the peaks of interest including those from the spinels.

Figure Fig. 3 SGIXD spectra over the 2θ range 17° to 21° of specimens following exposure over the heating rates shown and cooled to room temperature, including the spectrum obtained from the un-oxidised alloy, the locations for the dominant peaks for the oxides of interest are

shown.

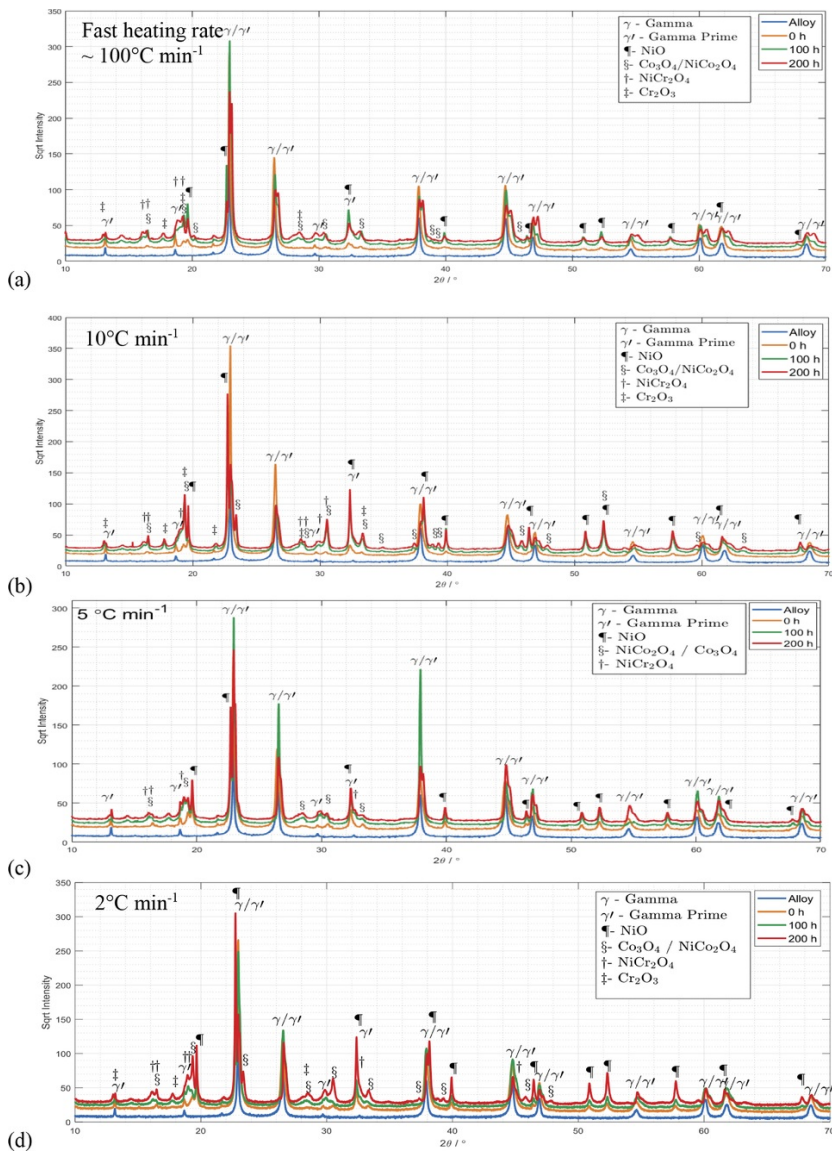The major peak positions for alumina (Al_2O_3) and rutile (TiO_2), oxides known to form on this alloy, are found at 2θ positions of 18.6° & 13.6° and 14.56° & 19.05°, respectively. Neither of these phases were positively identified in any of the spectra obtained in this study.

The intensities of the peaks associated with the γ/γ′ remained relatively constant for each specimen, Fig. 2. In Fig. 3 the peak at 2θ of 18.7° appears larger on the specimens after the heating stage compared to the unoxidised specimen. This may be due to the formation of $NiCr_2O_4$, (013) reflection Table 3, however, there clearly is not a peak forming associated with the 100% (121) reflection at 19.1°. Thus, the difference in peak intensity may be due to differences in alignment of the specimens in the path of the X-ray beam. The similarity in the height of the peak at 18.7°, present in the specimens following the heating stage, enables comparisons of changes in the relative heights of the other peaks present, Fig. 3. For instance, examination of the NiO/CoO peak at 2θ of 19.7° showed that this oxide was present on all specimens after the heating stage and that the relative height increased with decreasing heating rates. This indicated that NiO/CoO was forming on the surface of this alloy during low temperature exposure and thus the relative quantity increased with the increased thermal exposure time associated with the slower heating rates. The Co_3O_4/$NiCo_2O_4$ peak, at a 2θ of 19.3°, showed a similar trend although the intensity was less than that observed for NiO/CoO. No evidence of $NiCr_2O_4$ or Cr_2O_3 formation was seen during the heating stage.

3.2 Effect of heating rate on extended thermal exposure

A series of spectra obtained from specimens exposed to 650 °C for increasing time, up to 200 h~~200 hours~~, at selected heating rates are presented in Fig. 4, (a) the fastest heating rate of ~100 °C·min^{-1}, (b) 10 °C·min^{-1}, (c) 5 °C·min^{-1} and (d) 2 °C·min^{-1}. In each case, the spectrum obtained from the un-oxidised alloy and that obtained after the heating stage only, shown in Fig. 3 and labelled here as 0 h~~0 hours~~, are included.

(a)

(b)

(c)

(d)

alt-text: Fig. 4

The oxides that had formed were the same in all cases, however, the relative intensities of the major peaks associated with these phases varied depending on heating rate, Fig. 5. No peaks associated with Al_2O_3 or TiO_2 were found in the spectra. Each spectrum was from an individual specimen and some level of specimen-to-specimen variation was expected. However, the following key trends were observed:

1. NiO/CoO formed in all cases during the heating stage. Following the fastest heating rate and at 40 °C min^{-1} the relative intensity of the NiO/CoO {111} peak at $2\theta = 19.7°$ after 200 h200 hours decreased, when compared to the 100 h condition. Following the heating

rates of 5 to 20 °C min^{-1} the intensity of the NiO/CoO peak remained constant relative to the intensity at 100 h~~100 hours~~. However, at the slowest heating rate the intensity of this peak increased with increasing time at 650 °C.

2. Co$_3$O$_4$/NiCo$_2$O$_4$ also formed during the heating stage in all cases. It appeared to decrease between 100 ~~to~~ and 200 h~~200 hours~~ exposure following the fastest heating rate and 40 °C min^{-1}. It increased following the heating rates of 20 °C min^{-1} but the intensities of the peaks remained mostly unchanged following the 10 and 5 °C min^{-1} heating rates and increased after the 2 °C min^{-1} heating rate.

3. NiCr$_2$O$_4$ formed during exposure at 650 °C and the relative intensities of the relevant peaks varied depending on the heating rate.

4. Cr$_2$O$_3$ formed during the prolonged exposure at 650 °C, however, it was not possible to obtain quantitative measurements of increased volume fraction with increasing time at temperature.

(a) Fastest ~ 100°C min^{-1} (b) 40°C min^{-1} (c) 20°C min^{-1}

(d) 10°C min^{-1} (e) 5°C min^{-1} (f) 2°C min^{-1}
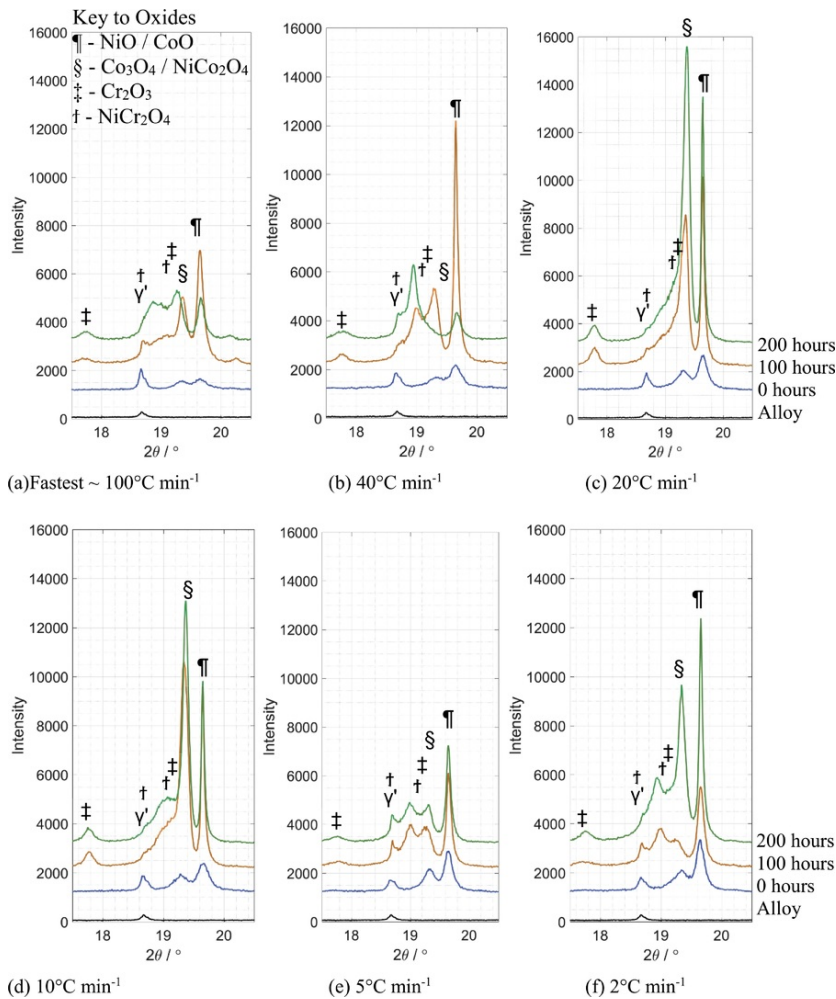
~~Figure~~ **Fig.** 5 SGIXD spectra over the 2θ range of 17 to 21° for specimens exposed to increasing time at 650 °C, up to 200 h~~200 hours~~, following the heating stage which were at rates of (a) ~100 °C min^{-1}, (b) 40 °C min^{-1}, (c) 20 °C min^{-1}, (d) 10 °C min^{-1}, (e) 5 °C min^{-1} and (f) 2 °C min^{-1}, showing changes in the oxides forming with increasing time at temperature. Spectra of the un-oxidised alloy and after the heating stage (labelled as 0 h~~0 hours~~) are included.

alt-text: Fig. 5

3.3 SEM evaluation of the surface of the specimens.

SEM examination of the surface of the samples after the controlled heating stage showed that a surface oxide had formed. The thinnest was evident in the ability to observe surface polishing scratches and individual alloy grains, Fig. 6(a). At higher magnification a patch-like pattern to the oxides appeared with dark or light contrast features of approximately 0.2 μm diameter, Fig. 6(b) and (c), within a medium contrast surface oxide. The light contrast features were precipitates in the alloy, rich in the heavier elements present. A more uniform coverage of oxide was observed on the specimens experiencing the slowest heating rate of 2 °C min^{-1}, Fig. 6(d) but still containing the light contrast phases.
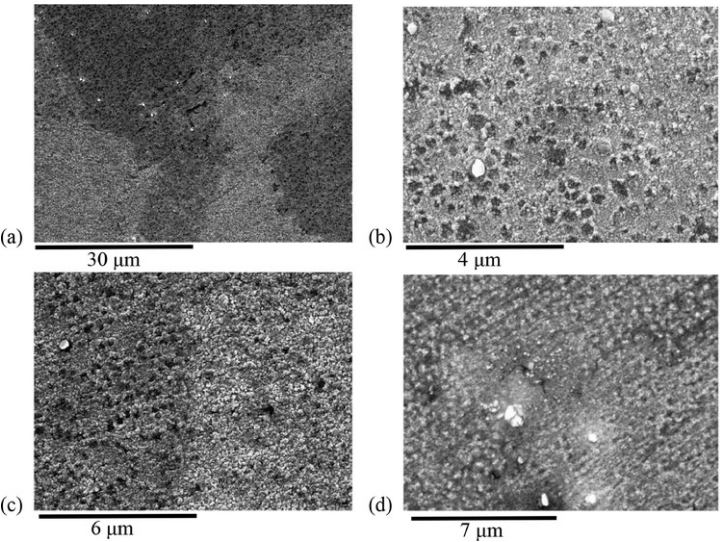
Fig. 6 SEM images of surface observations of selected specimens after the heating stages of (a) 20 °C min^{-1}, (b) fastest ~100 °C min^{-1}, (c) 5 °C min^{-1} and (d) 2 °C min^{-1}, showing variability in contrast of surface oxides at a micrometre scale, surface marks from polishing and differentiation of alloy grains due to oxide growth orientation effects.

alt-text: Fig. 6

Focused Ion Beam, FIB, milling was performed on selected specimens following the 200 h thermal exposure, Fig. 7. This revealed differences in the thicknesses of the surface oxides formed. At the heating rate of 20 °C min^{-1}, Fig. 7(a), a uniform coverage of approximately 0.08 +/- 0.01 μm was found, determined from 12 locations, with crystallites distributed across the surface. A planar interface between the oxide and the alloy was observed. The 200 h exposure following the heating rate of 5 °C min^{-1}, Fig. 7(b), showed a surface oxide of between 1.0 +/- 0.22 μm with a serrated outer surface and a planar interface with the alloy. For a 200 h thermal exposure following the slowest heating rate, 2 °C min^{-1}, Fig. 7(c), a surface oxide ranging in thickness from 0.6 μm at emergent grain boundaries to 1.5 +/- 0.2 μm over the remainder of the grain surface had formed. On close examination of the section a dual layer of oxide could be discerned, distinguishable due to the slight difference in contrast. The outer surface was relatively smooth but the interface with the alloy shows that the underlying oxide was growing into the alloy, shown in the change of profile of that interface. This effect was clearly noticeable for the specimen following the slow, 2 °C min^{-1}, heating stage followed by 1000 h thermal exposure at 650 °C, Fig. 7(d). The thin, protective oxide formed at the grain boundaries could be used to assess the direction of growth of each layer across the remainder of the surface. This showed that the outer oxide layer was outwardly growing while the inner layer was growing into the alloy. Examination using EDS analysis of the elemental profiles formed after 1000 h exposure, Fig. 8, revealed compositionally different oxide layers. The outer layer was rich in nickel and cobalt, i.e. the NiO/CoO phase, and the inner was more compositionally complex comprising all of the elements within the alloy. No evidence of a simple $Co_3O_4/NiCo_2O_4$ spinel was found; although this crystal structure was found using SGIXD. It may be surmised that a far more complex chemistry of this phase is forming. The profiles into the alloy showed no elemental depletion consistent with inwardly growing mixed composition oxides.
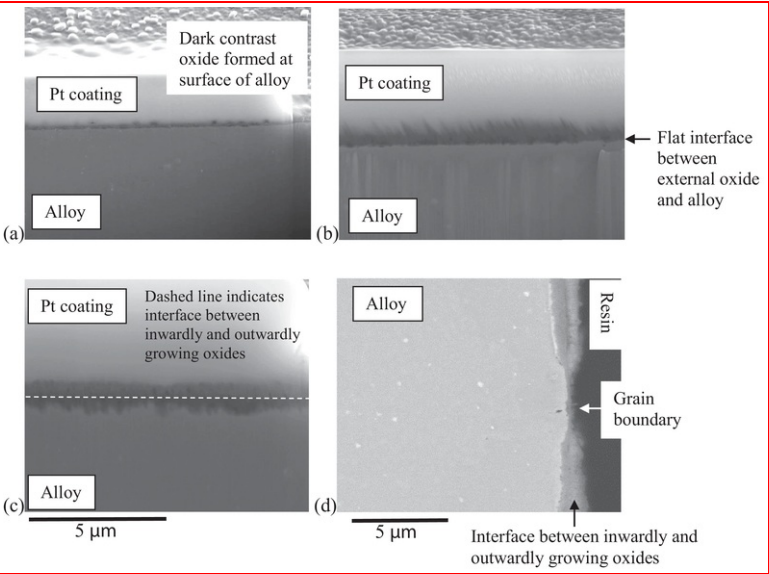
Figure Fig. 7 SEM images of FIB sections taken through selected specimens after a total of 200 h 200 hours exposure following heating rates of (a) 20 °C min^{-1}, (b) 5 °C min^{-1}, and (c) 2 °C min^{-1}, also (d) specimen after exposure for 1000 h 1000 hours at 650 °C following the 2 °C min^{-1} heating rates and prepared by mechanical sectioning, showing differences in surface oxide thickness and profile of oxide/alloy interfaces.

alt-text: Fig. 7
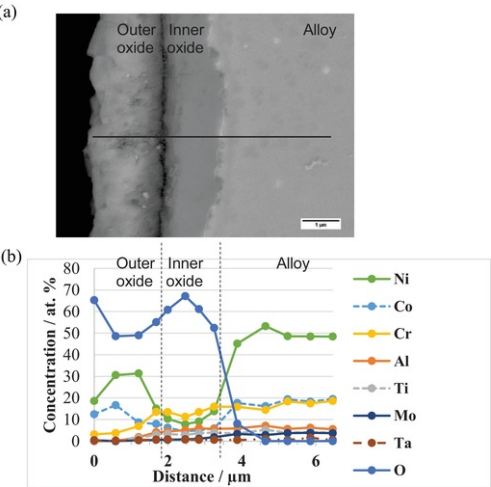
Figure Fig. 8 (a) SEM image of a cross-section through the specimen exposed to 650 °C for 1000 h 1000 hours following the heating rate of 2 °C min^{-1} with (b) EDS profiles, taken from the site indicated above, showing the compositional differences between the dual surface oxide layer and no development of a depletion profile into the alloy.

alt-text: Fig. 8

3.4 Thermodynamic considerations of oxide formation

Fully understanding the oxidation processes requires consideration of the thermodynamic stability of the candidate oxides formed. Possible oxidation reactions for this study are presented below and include reactions resulting

in spinel formation. These reactions, normalised to 1 mol of O_2, are;

$$2\ Ni\ +\ O_2\ \rightarrow\ 2\ NiO \#(A) \quad \text{[A1]}$$

$$2\ Co + O_2 \rightarrow 2\ CoO \#(B) \quad \text{[A2]}$$

$$4/3 Cr\ +\ O_2\ \rightarrow\ 2/3\ Cr_2O_3 \#(C) \quad \text{[A3][A4]}$$

$$3/2\ CoO\ +\ 1/4O_2\ \rightarrow\ 1/2\ Co_3O_4 \#(D) \quad \text{[A5]}$$

$$1/2\ NiO\ +\ 1/2\ Cr_2O_3\ \rightarrow\ 1/2\ NiCr_2O_4 \#(E) \quad \text{[A6]}$$

$$1/2\ NiO\ +\ 3/4\ O_2\ +\ Cr\ \rightarrow\ 1/2\ NiCr_2O_4 \#(F) \quad \text{[A7]}$$

$$2\ NiO\ +\ Cr\ \rightarrow\ 1/2\ NiCr_2O_4 + 3/2\ Ni \#(G) \quad \text{[A8]}$$
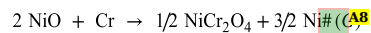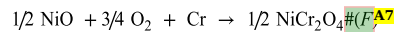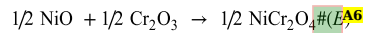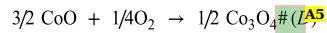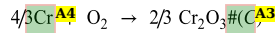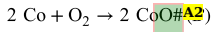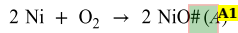
Annotations:

A1. Remove the "#" symbol and right align letter (A)

A2. Remove the "#" symbol and right align letter (B)

A3. Remove the "#" symbol and right align letter (C*)

A4. iNCLUDE A SPACE BETWEEN 4/3 AND Cr

A5. Remove the "#" symbol and right align letter (D) iNCLUDE A SPACE BETWEEN THE 1/4 AND THE O2

A6. Remove the "#" symbol and right align letter (E)*

A7. Remove the "#" symbol and right align letter (F)**

A8. Remove the "#" symbol and right align letter (G)

In most of the reactions above, the pO_2 can be fixed for a gaseous environment of air, the conditions of the experiments. For some reactions, the formation of the oxide relied on or may be constrained by, the formation of other oxides. Where applicable (i.e., C, E and F) adaptions were made in the calculation thus:-

- **(Replace bullet point with a "*".)** The formation of Cr_2O_3 was considered as either forming on the exposed surface and reliant on the atmospheric oxygen partial pressure, denoted in this paper as reaction (Ca), or forming underneath an already formed NiO layer, where oxygen partial pressure would be controlled by the NiO dissociation pressure, denoted as reaction (Cd). Similarly, for the spinel formation in reaction (E). (Ea) used a pO_2 value for the reactions leading to the formation of the spinel as atmospheric oxygen and (Ed) as a result of a solid state reaction between NiO and Cr_2O_3 formed via (Cd)

- **(Replace bullet point with "**".)** For reaction F it is assumed that the spinel forms by a reaction between NiO, elemental Cr and gaseous O_2; it was assumed that this reaction occurred at the base of the NiO layer and that the oxygen partial pressure at this site would be controlled by the NiO dissociation pressure.

An additional reaction route resulting in the formation of the spinel, $NiCr_2O_4$, from the individual elements has been identified:-

$$1/2\ Ni\ +\ Cr\ +\ O_2\ \rightarrow\ 1/2\ NiCr_2O_4 \#(H) \quad \text{[A1]}$$
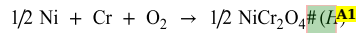
Annotations:

A1. Remove the "#" symbol and right align letter (H)

However, it is generally accepted that the formation route of $NiCr_2O_4$ is via the solid state reaction involving NiO with either Cr_2O_3 or Cr from the alloy, Reactions E, F or G. The evidence obtained in this investigation from the SGIXD showed the early formation of NiO/CoO and thus the reaction shown in H is unlikely to be occurring and will be excluded from further discussion here.

The thermodynamic favourability of all these reactions has been evaluated using a standard thermodynamic approach where the standard Gibbs free energy of reaction, at a given temperature, T, is calculated for pure substances by:

$$\Delta G_{r,T}^{\ominus} = \sum_{products} \Delta G_{f,T}^{\ominus} - \sum_{reactants} \Delta G_{f,T}^{\ominus} \qquad (1)$$

where $\Delta G_{r,t}^{\ominus}$ is the standard Gibbs free energy of reaction at a given temperature, T, for pure elements and $\Delta G_{f,T}^{\ominus}$ is the standard Gibbs free energy of formation for the products and reactants, at temperature, T, based on:

$$\Delta G_{f,T}^{\ominus} = \Delta H_f^{\ominus} - T\Delta S_f^{\ominus} \qquad (2)$$

where $\Delta H_f^{\ominus}$ and $\Delta S_f^{\ominus}$ are the standard enthalpies and entropies of formation, respectively.

In the case of alloys, where elements do not exist in their standard states the thermodynamic activities of elements cease to be unity, and thus:

$$\Delta G_{r,T} = \Delta G_{r,T}^{\ominus} + RT\ln K \qquad (3)$$

where the standard Gibbs free energy change of reaction is adjusted to give the Gibbs free energy change, $\Delta G_{r,\ T}$, by the molar gas constant, R, temperature, T, and the equilibrium constant, K, which for the reaction $2x/y\text{M}$ **A1** $+ \ \text{O}_2\ (g) \rightarrow 2/y\text{M}_x\text{O}_y\ (s)$ is given as:

$$K = \frac{a_{M_xO_y}^{2/y}\ \textbf{A2}}{a_M^{2x/y}\ a_{o_2}} \qquad (4)$$

where a_i is the thermodynamic activity of component, i, which for a pure substance is unity and for a gaseous species is equal to the partial pressure of that species.

The Gibbs free energies for each reaction A to G, were calculated using standard thermodynamic data, Table 4, [47,48] and temperature-dependent thermodynamic activities calculated for this alloy using Thermo-Calc and the TCNI8 database, Table 5. Reactions for Cd and Ed use the pO_2 value in equilibrium with the dissociation pressure of NiO, Table 6.

Table 4 Free energies for the relevant elements and oxides, [47,48].

alt-text: Table 4

T (K)	$\Delta G_{f,T}^{\ominus}$ (kJ mol^{-1})								
	Ni	NiO	Cr	Cr_2O_3	Co	CoO	Co_3O_4	$NiCr_2O_4$	O_2
300	−8.96	−252.00	−7.13	−1154.03	−9.01	−254.78	−935.75	−1277.28	−61.51
400	−12.37	−256.53	−9.88	−1163.84	−12.41	−260.91	−948.05	−1244.08	−82.48
500	−16.49	−262.38	−13.25	−1176.50	−16.48	−268.36	−963.92	−1210.88	−104.22
600	−21.21	−269.45	−17.15	−1191.52	−21.12	−276.88	−982.91	−1177.68	−126.60
700	−26.49	−277.41	−21.51	−1208.56	−26.26	−286.31	−1004.66	−1144.48	−149.51
800	−32.24	−286.13	−26.28	−1227.36	−31.91	−296.51	−1028.90	−1111.28	−172.88
900	−38.38	−295.52	−31.42	−1247.71	−37.97	−307.42	−1055.42	−1078.08	−196.67
1000	−44.89	−305.51	−36.92	−1269.46	−44.43	−318.94	−1084.07	−1044.88	−220.83
1100	−51.73	−316.06	−42.74	−1292.48	−51.25	−331.04	Unstable	−1011.68	−245.33

Table 5 Thermodynamic activities [49] based on composition of alloy and pO_2 values at equilibrium with NiO formation.

T (K)	Thermodynamic activity, a		
	Ni	Cr	Co
300	0.01046	0.05900	0.01032
400	0.01022	0.04635	0.01026
500	0.00744	0.03125	0.00969
600	0.00464	0.01930	0.00888
700	0.00326	0.01408	0.00557
800	0.00246	0.01006	0.00344
900	0.00181	0.00774	0.00223
1000	0.00134	0.00609	0.00147
1100	0.00099	0.00498	0.00096

Table 6 Calculated pO_2 values at equilibrium with NiO formation.

T (K)	Equilibrium pO_2 at alloy/NiO interface
300	1.08×10^{-70}
400	9.59×10^{-50}
500	5.87×10^{-37}
600	2.92×10^{-28}
700	4.81×10^{-22}
800	2.25×10^{-17}
900	1.13×10^{-13}
1000	1.13×10^{-10}
1100	3.61×10^{-08}

The calculated Gibbs free energy change for the reactions A to G are presented in Fig. 9. This shows the relative stabilities of each potential oxide when equilibrium is reached and demonstrates the effect of changing the pO_2 to accommodate the reaction path to the final oxide state for Cr_2O_3 and $NiCr_2O_4$, reactions C and E, respectively.

Legend for figure:
- (A) 2 Ni + O$_2$ -> 2 NiO
- (B) 2 Co + O$_2$ -> 2 CoO
- (Ca) $^4/_3$ Cr + O$_2$ -> $^2/_3$ Cr$_2$O$_3$ (atm)
- (Cd) $^4/_3$ Cr + O$_2$ -> $^2/_3$ Cr$_2$O$_3$ (NiO diss)
- (D) $^3/_2$ CoO + ¼ O$_2$ -> ½ Co$_3$O$_4$
- (Ea) ½ NiO + ½ Cr$_2$O$_3$ -> ½ NiCr$_2$O$_4$ (atm)
- (Ed) ½ NiO + ½ Cr$_2$O$_3$ -> ½ NiCr$_2$O$_4$ (NiO diss)
- (F) ½ NiO + Cr + ¾ O$_2$ -> ½ NiCr$_2$O$_4$
- (G) 2 NiO + Cr -> ½ NiCr$_2$O$_4$ + $^3/_2$ Ni
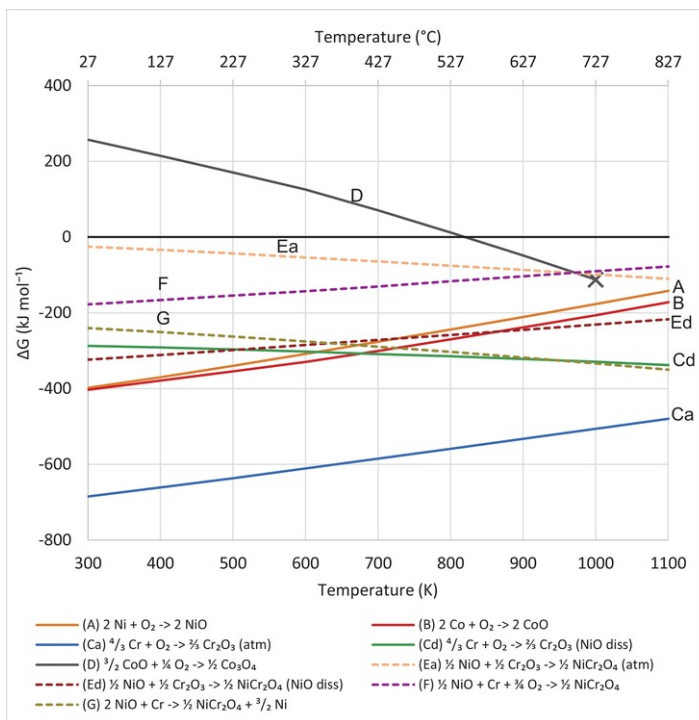
~~Figure~~ Fig. 9 Plots of free energies of reaction against temperature for reactions A to G. Reactions for binary oxides are shown as solid lines and those for NiCr$_2$O$_4$ are dashed lines. The trends can be used to identify the relative stability of each reaction, where only those with a negative free energy of formation are possible.

alt-text: Fig. 9

The approach taken to determine the free energy of formation of each of the reactions given, and plotted in Fig. 9, demonstrated the effect of pO_2 on the thermodynamic stability of the reactions A to G. The thermodynamic favourability of Reaction Ca changes significantly when Cr$_2$O$_3$ forms at the interface of NiO and the alloy, bringing it closer to that of the spinel reaction G. Conversely, for Reaction E, formed under the lower pO_2 conditions at the same interface, this spinel reaction becomes more stable. The calculations shows that at 650 °C there are a number of reactions of similar stability that could form from this alloy where a NiO has formed on the surface.

Oxides of aluminium and titanium are also expected to form in this alloy system:-
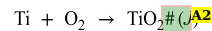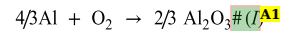
$$4/3 Al + O_2 \rightarrow 2/3\ Al_2O_3 \#(I \text{ [A1]}$$

$$Ti + O_2 \rightarrow TiO_2 \#(J \text{ [A2]}$$

The calculated values of $\Delta G_{r,T}$ for Al$_2$O$_3$ at 650 °C (923 K) were: -720 kJ mol^{-1} in atmospheric air, -510 kJ mol^{-1} in equilibrium with NiO, and -190 kJ mol^{-1} in equilibrium with Cr$_2$O$_3$. For TiO$_2$ a value of -650 kJ mol^{-1} was calculated using atmospheric oxygen as this phase formed at the outer surface. Neither of these oxides were detected in this study, possibly due to the low volume fractions formed or, as in the case of Al$_2$O$_3$, the site of formation, i.e., internally.

It is important to note that the calculated Gibbs free energy values are based on thermodynamic data for the formation of pure oxides. There are likely to be minor variations in these values as oxides formed in an alloy system

are rarely pure and stoichiometric, where the actual free energies of formation and activities of the oxide phases will reflect this. However, the approach taken, in assuming unity for the oxide formed and accounting for the effect on activities of elements from the alloy and the influence of differing pO_2, demonstrates the principle effects on the stability of the oxides formed under equilibrium conditions.

4 Discussion

This study provides clear evidence that the oxidation process begins during the heating stage and the subsequent long exposure is influenced by the heating rate. The SGIXD spectra showed the formation of NiO/CoO and Co_3O_4/$NiCo_2O_4$ across all specimens independent of heating rate, Figs. 2 and 3. The relative concentrations, based on the intensity of the major peaks, increased with decreasing heating rate, i.e. increased thermal exposure at lower temperatures. Exact concentration values for the oxides formed could not be determined as the data was not collected from a standardised interaction volume. However, qualitative comparisons could be made based on intensities, providing an unambiguous method to track previously unobserved oxide reaction sequences and oxide development.

The processes of oxide formation observed during the heating stage were transient and did not follow the predictions based on thermodynamic calculations, of the type presented in Fig. 8. (This should be Fig. 9.) Under equilibrium conditions Cr_2O_3 would be the expected preferentially formed oxide on this alloy, following reaction Ca. However, no peaks associated with Cr_2O_3 were seen to form during the heating stage, Fig. 3. This was in agreement with studies on the early stages of oxidation on binary alloys where it was shown that the first oxides formed were nickel, nucleated as islands distributed across the surface of the specimen [4–7]. It has also been shown that a metastable chromium-oxygen phase formed on the surface of binary alloys, surrounding the NiO islands [5-9]. Examination of the surface of the specimens after the heating stage, Fig. 6, showed dark contrast islands within lighter contrast oxides; indicating a change in composition of the two sites perhaps as a result of island formation. The reduction in the number of dark contrast features at the slowest heating rates may have been due to the faster outward and lateral growth of some of the oxides which grew over the slower growing oxides [7,29,50].

Early formation of Cr_2O_3 at emergent grain boundaries is also known to occur where these fast paths promote diffusion of chromium to the surface, as shown in ~~ref~~ Ref. [31]. However, the slow growth of this oxide [50] and the quantities formed at grain boundaries, during the heating stage, would be too small to detect using this technique. The data obtained from the SGIXD has clearly shown that less thermodynamically stable oxides formed across the surface of the alloy in sufficient quantities to be detected and thus demonstrates the importance of the kinetics of this growth in the establishment of the surface oxide.

During the fastest two heating stages it can be envisaged that the thinnest oxide coverage was achieved, Fig. 7. The SGIXD spectra showed that once at 650 °C the more thermodynamically stable oxides of Cr_2O_3 and $NiCr_2O_4$, potentially following reactions Ca, Cd and G, developed with a reduction in NiO/CoO and Co_3O_4/$NiCo_2O_4$. This replicates the oxidation behaviour previously reported for this alloy [12] and follows the models proposed for this alloy type [10,23,29,30,51] with the more stable Cr_2O_3 spreading laterally from, for instance, emergent grain boundaries, to eventually form a continuous layer, thus restricting the supply of Ni and Co to the outer surface and slowing further growth, shown schematically in Fig. 10(a). In this study, the location of the Cr_2O_3 peaks corresponds to the location for an undoped, pure form of the crystal. Doping with titanium, for example, is known to shift peaks [52]. Thus, it may be surmised that doping of Cr_2O_3 by titanium, reported to occur in this and similar alloys [33,53] does not occur within the first few hundred hours at 650 °C. It is inferred that SGIXD can potentially detect the onset of doping-related lattice parameter changes and could complement other work on the role of Ti and other elements in such alloys [54].
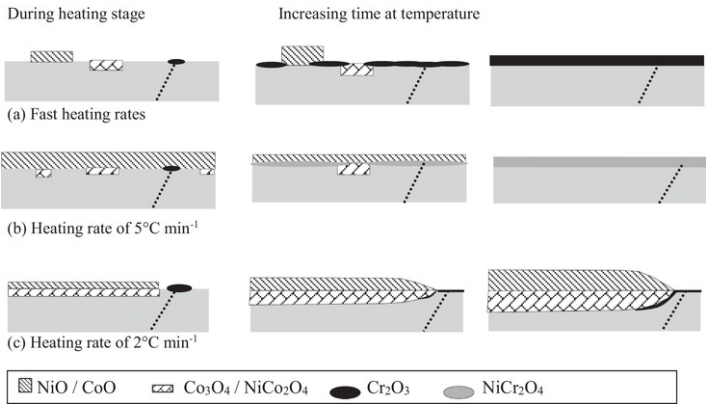
Figure Fig. 10 Series of schematic diagrams describing the formation of oxides on the nickel-based superalloy, RR1000, resulting from the following heating rates: (a) fast heating rate >40 °C min^{-1}, (b) 5 °C min^{-1} and (c) 2 °C min^{-1}. Location of a grain boundary is indicated by a dashed line, these are paths of faster diffusion of elements from the bulk to the surface, e.g. chromium to form Cr_2O_3.

alt-text: Fig. 10

At the heating rates of 20 and 10 °C·min^{-1} the SGIXD data showed significant growth of the NiO/CoO and Co$_3$O$_4$/NiCo$_2$O$_4$ during exposure at 650 °C for up to 200 h~~200 hours~~, Fig. 5. Cr$_2$O$_3$ and NiCr$_2$O$_4$ were also shown to form but the quantities of the former oxides continued to dominate. This implies that a significant proportion of the surface of the specimens was covered by less protective oxides, preventing the establishment of the more protective Cr$_2$O$_3$ via reaction Ca, Fig. 8 (Replace with Fig. 9.). Instead, this reaction becomes less thermodynamically stable, see reaction Cd where the pO_2 is in equilibrium with the overlying NiO. As further information is needed no schematic has been include in Fig. 10.

The SGIXD data did provide insight into the oxide formation sequence following the 5 °C·min^{-1} heating rate, Figs. 3 and 5, i.e. the surprising formation of a dominant, protective surface oxide of NiCr$_2$O$_4$ which initiated this systematic investigation [33]. SGIXD spectra, Fig. 5, showed the formation of the NiCr$_2$O$_4$ phase within the first 100 h exposure at 650 °C. NiO/CoO and Co$_3$O$_4$/NiCo$_2$O$_4$ also continued to form but remained constant after a further 100 h~~100 hours~~ exposure. It is proposed that NiCr$_2$O$_4$ dominates due to the number of available reaction paths that leads to its formation. In Fig. 8 (Replace with Fig. 9.) Reactions E, F and G all lead to NiCr$_2$O$_4$ formation with Reaction G being thermodynamically equivalent to Reaction Cd. A schematic of this path is given in Fig. 10(b) and additional testing will be required to assess at what time the NiCr$_2$O$_4$ becomes the dominant oxide.

The highly beneficial effect observed following the heating rate of 5 °C·min^{-1} contrasted with the devastating finding at 2 °C·min^{-1}. SGIXD showed the continued growth of the NiO/CoO and NiCo$_2$O$_4$/Co$_3$O$_4$ phases during exposure at 650 °C, Fig. 5. FIB sectioning showed the development of a dual oxide layer with an outwardly growing oxide underlaid by an inwardly growing layer; EDS analysis revealed the difference in the compositions of the two layers and showed no elemental depletion of the underlying alloy. This dual layer formation and change in profile of the oxide alloy interface was not seen at faster heating rates. The effect of the inwardly growing oxide was evident in the FIB cross-section by a loss of the flat profile, which can be seen in Fig. 7(c) and this effect was made clearer after 1000 h~~1000 hours~~ exposure, Fig. 7(d). Here the role of emergent grain boundaries as sites for the formation of a protective surface layer of Cr$_2$O$_3$, can be seen. These can be used to locate the position of the original surface of the specimen thus emphasising the extent of the inward and outward growth across the remainder of the surface. Further analysis of the two oxides is ongoing but the chemistries are complex with the outer oxide containing Ni and Co oxides and the inner consisting of oxides comprising all elements of the alloy. The development of oxides resulting from a slow heating rate are shown schematically in Fig. 10(c).

A study performed on the binary system Ni-20Cr using a heating rate of 5 K·min^{-1}, [30], showed some similarities to the findings here at the lower temperatures used in that study, i.e. 500 and 600 °C. Cr$_2$O$_3$ formed preferentially at emergent grain boundaries and also as discontinuous particles across the surface, underneath a growing NiO layer. Eventually, after approximately 2 h~~2 hours~~ at 600 °C, a continuous layer of mixed oxides, including Cr$_2$O$_3$ and NiCr$_2$O$_4$, formed across the surface underneath the NiO. ~~It was stated there that this~~ This demonstrated that the chromium content was not sufficient to form a surface Cr$_2$O$_3$ except at grain boundaries, at these temperatures. At higher temperatures in that study, i.e. 700 to 900 °C, a more continuous inwardly growing layer of NiCr$_2$O$_4$ was reported. This was not considered protective but appeared to be similar to the behaviour seen in this study by the specimens experiencing the 2 °C·min^{-1} heating rate, i.e. protective oxidation at the emergent grain boundaries with significant inward and outward growth of a spinel and NiO, respectively, across the remainder of the surface. The permeability of oxygen into the alloy was observed at 600 °C with the formation of internal precipitates of Cr$_2$O$_3$ but not at 500 °C indicating the influence of temperature on this parameter. The differences in the finding between this study and that reported by Calvarin et al. [30] may be attributed to the role of alloying elements, affecting parameters such as the permeability of oxygen in the alloy or the stability of the oxide phases formed.

The focus of this investigation was to study the effect of heating rate on the oxide sequences up to 200 h~~200 hours~~ exposure at 650 °C using SGIXD. The intriguing heating rate dependent oxide reaction sequences are summarised schematically in Fig. 9. Further testing is needed in some areas but the evidence does provide new insights into the development of a protective NiCr$_2$O$_4$ layer following a heating rate of 5 °C·min^{-1}. The formation of the spinel is known to occur in the nickel-based alloy system but usually the layer is discontinuous or particulate in nature [19,20,22–24,29–31]. An explanation for the persistence of so complete a NiCr$_2$O$_4$ layer across the surface of the specimens may be due to the number of possible thermodynamically favourable reaction routes available, Fig. 9. The influence of other alloying elements on the stability of the oxide also needs ~~also~~ to be considered, e.g. molybdenum has been shown to stabilise this oxide on simple nickel alloys [9] and is present in the current alloy, Table 1.

Another effect on the development of a continuous surface layer may be the retention of a flat interface between the oxide and the alloy, Fig. 7(b). The retention of a planar interface up to 4000 h~~4000 hours~~ at 650 °C was demonstrated in ~~ref~~ Ref. [33]. This may be key to the endurance of the NiCr$_2$O$_4$ layer. At higher temperatures the interface of this alloy loses its original planar topography [12,16], possibly a consequence of the internal oxidation of aluminium and associated depletion of the γ′ precipitate phase. Work is ongoing to investigate whether the same beneficial effect of using a 5 °C·min^{-1} heating rate is observed at higher temperatures but early tests suggest it is not the case.

SGIXD has been successfully used in this study to track the reaction paths in oxide formation. The results showed that there was a zone of heating rates around the 5 °C·min^{-1}, during which the right amount of oxide formed to provide the precursor to the formation of a continuous surface layer of NiCr$_2$O$_4$ on exposure at 650 °C. Whilst further testing will refine the findings, the use of SGIXD has provided new information on phase constituents of the thin oxide films formed and also the associated role of heating rate.

5 Conclusions

Synchrotron GIXRD has been successfully used to track the oxide formation occurring during the heating stage and subsequent transient oxidation stage with the following findings:

- NiO/CoO and Co_3O_4/$NiCo_2O_4$ formed during all the heating stages investigated.

- At the fastest heating rates used Cr_2O_3 formation was able to dominate the oxidation reactions within the first 100 h at 650 °C, following the oxidation behaviour already established for this alloy type.

- Over the range 20 to 10 °C min^{-1} the oxidation behaviour diverged from that expected with the continued formation of NiO/CoO and Co_3O_4/$NiCo_2O_4$ oxides. Further testing has been proposed to assess whether a protective layer of Cr_2O_3 eventually forms and dominates beyond the 200 h thermal exposure.

- At the slowest heating rate of 2 °C min^{-1} a non-protective surface layer formed, consisting of a dual layer of an outwardly growing NiO/CoO underlaid by an inwardly growing mixed oxide.

- The results showed that there is a zone within the heating rates investigated, at ~5 °C min^{-1}, where just the right amount of precursor oxide formed during the heating stage to aid the development of a continuous surface layer of $NiCr_2O_4$. A number of factors are proposed to aid in this behaviour, e.g., numerous reaction routes available leading to the formation of $NiCr_2O_4$ and the maintenance of a planar surface.

Further testing is envisaged where the ability of SGIXD to resolve spectra from thin surface oxide films is expected to provide the insight required for greater understanding.

Declaration of Competing Interest

The authors declare that they have no known competing financial interests or personal relationships that could have appeared to influence the work reported in this paper.

Acknowledgements

Supplementary material

Supplementary material associated with this article can be found, in the online version, at doi:10.1016/j.actamat.2019.10.019.

References

[1] F. Pettit, R. Yinger and J.B. Wagner, Jr., The mechanism of oxidation of iron in carbon monoxide-carbon dioxide mixtures, *Acta Metall.* **8**, 1960, 617–623.

[2] J.T. Stuckless, C.E. Wartnaby, N. Al-Saraf, St.J.B. Dixon-Warrant, M. Kovar and D.A. King, Oxygen chemisorption and oxide film growth on Ni{100}, {110}, and {111}: sticking probabilities and microcalorimetric adsorption heats, *J. Chem. Phys.* **106**, 1997, 2012–2030.

[3] J.C. Yang, M. Yeadon, B. Kolasa and J.M. Gibson, The homogeneous nucleation mechanism of Cu_2O on Cu(001), *Scr. Mater.* **38**, 1998, 1237–1242.

[4] P.H. Holloway and J.B. Hudson, Kinetics of the reaction of oxygen with clean nickel single crystal surfaces, *Surf. Sci.* **43**, 1974, 123–140.

[5] W.H. Blade and P. Reinke, From alloy to oxide: capturing the early stages of oxidation on Ni–Cr(100) alloys, *ACS Appl. Mater. Interfaces* **10**, 2018, 43219–43229.

[6] R. Ramanathan, G. Ramalingam, J. Perepezko, P. Reinke and P.W. Voorhees, Evolution of NiO island size distributions during the oxidation of a Ni-5Cr alloy: experiment and modeling, *ACS Appl. Mater. Interfaces* **10**, 2018, 9136–9146.

[7] L. Luo, L. Zou, D.K. Schreiber, D.R. Baer, S.M. Bruemmer, G. Zhou and C.-M. Wang, In-situ transmission electron microscopy study of surface oxidation for Ni-10Cr and Ni–20Cr alloys, *Scr. Mater.* **114**, 2016, 129–132.

[8] J.S. Foord and R.M. Lambert, Oxygen chemisorption and corrosion on Cr(100) and Cr(110) single crystal surfaces, *Surf. Sci.* **161**, 1985, 513–520.

[9] X.-X. Yu, A. Gulec, C.M. Andolina, E.J. Zeitchick, K. Gusieva, J.C. Yang, J.R. Scully, J.H. Perepezko and L.D. Marks, In situ observations of early stage oxidation f Ni–Cr and Ni–Cr–Mo alloys, *Corrosion* **74**, 2018, 939–946.

[10] A. Atkinson, Transport processes during the growth of oxide films at elevated temperature, *Rev. Mod. Phys.* **57**, 1985, 437–470.

[11] A. Encinas-Oropesa, N.J. Simms, J.R. Nicholls, G.R. Drew, J. Leggett and M. Hardy, Evaluation of oxidation-related damage caused to a gas turbine disc alloy between 700 and 800 °C, *Mater. High Temp.* **26**, 2009, 223–232.

[12] M.P. Taylor, H.E. Evans, S. Stekovic and M.C. Hardy, The oxidation characteristics of the nickel-based superalloy, RR1000, at temperatures of 700–900 °C, *Mater. High Temp.* **29**, 2012, 145–150.

[13] S. Cruchley, H.E. Evans, M.P. Taylor, M.C. Hardy and S. Stekovic, Chromia layer growth on a Ni-based superalloy: sub-parabolic kinetics and the role of titanium, *Corros. Sci.* **75**, 2013, 58–66.

[14] S. Cruchley, M.P. Taylor, R. Ding, H.E. Evans, D.J. Childs and M.C. Hardy, Comparison of chromia growth kinetics in a Ni-based superalloy, with and without shot-peening, *Corros. Sci.* **100**, 2015, 242–252.

[15] S. Cruchley, M.P. Taylor, H. Li, H.E. Evans, P. Bowen, D.J. Childs and M.C. Hardy, Effect of prior oxidation on high cycle fatigue performance of RR1000 and role of oxidation in fatigue crack initiation, *Mater. High Temp.* **32**, 2015, 68–73.

[16] S. Cruchley, M.P. Taylor, H.E. Evans, M.C. Hardy and D.J. Childs, Characterisation of subsurface oxidation damage in Ni based superalloy, RR1000, *Mater. Sci. Technol.* **30**, 2014, 1884–1889.

[17] S. Cruchley, H.E. Evans and M.P. Taylor, An overview of the oxidation of Ni-based superalloys for turbine disc applications: surface condition, applied load and mechanical performance, *Mater. High Temp.* **33**, 2016, 465–475.

[18] H.E. Evans, A.T. Donaldson and T.C. Gilmour, Mechanisms of breakaway oxidation and application to a chromia-forming steel, *Oxid. Metals* **52**, 1999, 379–402.

[19] B. Chattopadhyay and G.C. Wood, The transient oxidation of alloys, *Oxid. Metals* **2**, 1970, 373–399.

[20] B.H. Kear, F.S. Pettit, D.E. Fornwalt and L.P. Lemaire, On the transient oxidation of a Ni–15Cr–4Al alloy, *Oxid. Metals* **3**, 1971, 557–569.

[21] J.L. Smialek and R. Gibala, Structure of transient oxides formed on NiCrAl alloys, *Metall. Trans. A* **14A**, 1983, 2143–2161.

[22] L. Hu, D.B. Hovis and A.H. Heuer, Transient oxidation of a γ-Ni-28Cr-11Al alloy, *Oxid. Metals* **73**, 2010, 275–288.

[23] C.S. Giggins and F.S. Pettit, Oxidation of Ni–Cr–Al alloys between 1000° and 1200 °C, *J. Electrochem. Soc.* **118**, 1971, 1782–1790.

[24] T.J. Nijdam, L.P.H. Jeurgens and W.G. Sloof, Promoting exclusive α-Al_2O_3 growth upon high-temperature oxidation of NiCrAl alloys: experiment versus model predictions, *Acta Mater.* **53**, 2005, 1643–1653.

[25] I.M. Edmonds, H.E. Evans, C.N. Jones, et al., Oxidation and coating evolution in aluminised fourth generation blade alloys, In: R.C. Reed, K.A. Green, et al., (Eds.), *Superalloys 2008,* 2008, TMS, Seven Springs; PA, 661–671.

[26] I.M. Edmonds, H.E. Evans and C.N. Jones, The role of the *γ′* precipitate dispersion in forming a protective scale on Ni-based superalloys at 750 °C, *Oxid. Metals* **73**, 2010, 193–206.

[27] C. Greskovich, Kinetics of $NiCr_2O_4$ formation and diffusion of Cr^{3+} ions in NiO, *J. Am. Ceram. Soc.* **53**, 1970, 498–502.

[28] G.Y. Liang, C. Zhu, X.Y. Wu and Y. Wu, The formation model of Ni-Cr oxides on NiCoCrAlY-sprayed coating, *Appl. Surf. Sci.* **257**, 2011, 6468–6473.

[29] G.C. Wood and B. Chattopadhyay, The transient oxidation of Ni-based alloys, *Oxid. Metals* **10**, 1970, 471–480.

[30] G. Calvarin, R. Moulins and A.M. Huntz, Oxidation mechanism of Ni–20Cr foil and this relation to the oxide-scale microstructure, *Oxid. Metals* **53**, 2000, 25–48.

[31] G.C. Wood and T. Hodgkiess, Mechanism of oxidation of dilute nickel-chromium alloys, *Nature* **211**, 1966, 1358–1361.

[32] X.X. Yu, A. Gulec, Q. Sherman, K. Lutton, J.R. Scully, J.H. Perepezko, P.W. Voorhees and L.D. Marks, Non-equilibrium solute capture in passivating oxide films, *Phys. Rev. Lett.* **121**, 2018, 145701, 1-7.

[33] T.D. Reynolds, M.P. Taylor, D.J. Child and H.E. Evans, The effect of elevated air pressure on the oxidation properties of the nickel-based superalloy, RR1000, at 650 °C with different surface modifications, *Mater. High Temp.* **35**, 2018, 130–140.

[34] S.J. Hessel, W. Voice, A.W. James, S.A. Blackham, C.J. Small, M.R. Winstone, (1997) Nickel Alloy for Turbine Engine Component. Patent no. EP 0803585 A1. [Online]. Available

at:https://www.google.com/patents/EP0803585A1?cl=en.

[35] S.P. Thompson, J.E. Parker, J. Marchal, J. Potter, A. Birt, F. Yuan, R.D. Fearn, A.R. Lennie, S.R. Street and C.C. Tang, Fast X-ray powder diffraction on I11 at Diamond, *J. Synchrotron Rad.* **18**, 2011, 637–648.

[36] G. Bergerhoff, I.D. Brown, et al., Crystallographic Databases, In: F.H. Allen, et al., (Eds.), 1987, International Union of Crystallography; Chester, (Hrsg.).

[37] D.M. Collins, L. Yan, E.A. Marquis, L.D. Connor, J.J. Ciardiello, A.D. Evans and H.J. Stone, Lattice misfit during ageing of a polycrystalline nickel-base superalloy, *Acta Mater.* **61**, 2013, 7791–7804.

[38] H. Sawada, Residual electron density study of chromium sesquioxide by crystal structure and scattering factor refinement, *Mater. Res. Bull.* **29**, 1994, 239–245.

[39] T. Oyama, Y. Iimura, T. Ishii and K. Takeuchi, Synthesis and crystal structure of chromium-titanium composite oxide fine particles by laser induced chain reaction, the chemical Society of Japan, *Chem. Ind. Chem.* **7**, 1993, 825–830.

[40] T. Mashimo, R. Bagum, Y. Ogata, M. Tokuda, M. Okube, K. Sugiyama, Y. Kinemuchi, H. Isobe and A. Yoshiasa, Structure of single-crystal Rutile (TiO_2) prepared by high-temperature ultracentrifugation, *Cryst. Growth Des.* **17**, 2017, 1460–1464.

[41] S. Sasaki, K. Fujino and Y. Takeuchi, X-ray determination of electron-density distributions in oxides, MgO, MnO, CoO, and NiO, and atomic scattering factors of their constituent atoms, *Proc. Jpn. Acad. Ser. B* **55**, 1979, 43–48.

[42] S. Kondo, K. Tateishi and N. Ishizawa, Structural evolution of corundum at high temperatures, *Jpn. J. Appl. Phys.* **47**, 2008, 616–619.

[43] J.P. Picard, G. Baud, J.P. Besse and R Chevalier, Croissance cristalline et étude structurale de CoO, *J. Less Common Met.* **75**, 1980, 99–104.

[44] G. Ueno, S. Sato and Y. Kino, The low-temperature tetragonal phase of $NiCr_2O_4$, *Acta Crystallogr.* **55**, 1999, 1963–1966, Section C.

[45] Y.-J. Gu, Y.-B. Chen, H.-Q. Liu, Y.-M. Wang, C.-L. Wang and H.-K. Wu, Structural characterization of layered $LiNi_{0.85}-x$MnxCo$_{0.15}$O$_2$ with x = 0, 0.1, 0.2 and 0.4 oxide electrodes for Li batteries, *J. Alloys Compd.* **509**, 2011, 7915–7921.

[46] K. Hirota, T. Inoue, N. Mochida and A. Ohtsuka, Study of germanium spinels (Part 3), *J. Ceram. Soc. Jpn.* **98**, 1990, 976–986.

[47] I. Barin and O. Knacke, Thermochemical Properties of Inorganic Substances, first ed., 1973, Springer-Verlag; Berlin, Germany.

[48] D.J. Young, High Temperature Oxidation and Corrosion of Metals, second ed., 2016, Elsevier Science; Amsterdam, Netherlands.

[49] J.O. Andersson, T. Helander, L. Höglund, P. Shi and B. Sundman, Thermo Calc & DICTRA, computational tools for materials science, *Calphad* **26**, 2002, 273–312.

[50] G. Salomonsen, N. Norman, O. Lonsjo and T.G. Finstad, Kinetics and mechanism of oxide formation on Cr thin films, *J. Phys. Condens. Matter* **1**, 1989, 7843–7850.

[51] Y. Unutulmazsoy, R. Merkle, D. Fischer, J. Mannhart and J. Maier, The oxidation kinetics of thin nickel films between 250 and 500 °C, *J. Phys. Chem.* **19**, 2017, 9045–9052.

[52] A. Atkinson, M.R. Levy, S. Roche and R.A. Rudkin, Defect properties of Ti-doped Cr_2O_3, *Sol. State Ion.* **177**, 2006, 1767–1770.

[53] A. Jalowicka, W. Nowak, D. Naumenko, L. Singheiser and W.J. Quadakkers, Effect of nickel base superalloy composition on oxidation resistance in SO_2 containing, high pO_2 environments, *Mater. Corros.* **65**, 2014, 178–187.

[54] S. Pedrazzini, B.S. Rowlands, A. Turk, I.M.D. Parr, M.C. Hardy, P.A.J. Bagot, M.P. Moody, E. Galindo-Nava and H.J. Stone, Partitioning of Ti and kinetic growth predictions of the thermally grown chromia scale of a polycrystalline nickel-based superalloy, *Metall. Mater. Trans. A* **50**, 2019, 3024–3029.

Appendix. Supplementary materials

Multimedia Component 1

Graphical abstract
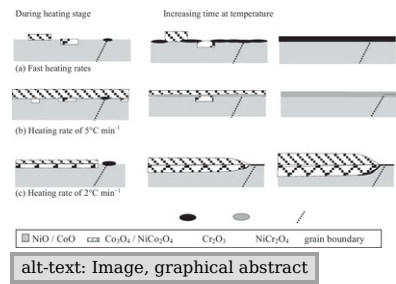
Queries and Answers

Query: Please confirm that givennames and surnames have been identified correctly.

Answer: Yes

Query: Please validate the author affiliation "c".

Answer: We confirm this double affiliation for S.R. Street and that they are both correct.